RSC Advances

ROYAL SOCIETY OF CHEMISTRY

PAPER

View Article Online
View Journal | View Issue

Cite this: *RSC Adv.*, 2023, **13**, 5859

Ultrasonic spray pyrolysis synthesis of TiO_2/Al_2O_3 microspheres with enhanced removal efficiency towards toxic industrial dyes

Thi Hong Anh Nguyen,[a] Duong Tuan Quang,[b] Le Van Tan[c] and The Ky Vo*[c]

Received 2nd January 2023
Accepted 3rd February 2023

DOI: 10.1039/d3ra00024a

rsc.li/rsc-advances

Developing low-cost and highly effective adsorbent materials to decolorate wastewater is still challenging in the industry. In this study, TiO_2-modified Al_2O_3 microspheres with different TiO_2 contents were produced by spray pyrolysis, which is rapid and easy to scale up. Results reveal that the modification of γ-Al_2O_3 with TiO_2 reduced the crystallite size of Al_2O_3 and generated more active sites in the composite sample. The as-synthesized Al_2O_3–TiO_2 microspheres were applied to remove anionic methyl orange (MO) and cationic rhodamine B (RB) dyes in an aqueous solution using batch and continuous flow column sorption processes. Results show that the Al_2O_3 microspheres modified with 15 wt% of TiO_2 exhibited the maximum adsorbing capacity of $\sim$41.15 mg g^{-1} and $\sim$32.28 mg g^{-1} for MO and RB, respectively, exceeding the bare γ-Al_2O_3 and TiO_2. The impact of environmental complexities on the material's reactivity for the organic pollutants was further delineated by adjusting the pH and adding coexisting ions. At pH $\sim$5.5, the TiO_2/Al_2O_3 microspheres showed higher sorption selectivity towards MO. In the continuous flow column removal, the TiO_2/Al_2O_3 microspheres achieved sorption capacities of $\sim$31 mg g^{-1} and $\sim$19 mg g^{-1} until the breakthrough point for MO and RB, respectively. The findings reveal that TiO_2-modified Al_2O_3 microspheres were rapidly prepared by spray pyrolysis, and they effectively treated organic dyes in water in batch and continuous flow removal processes.

1. Introduction

Organic dyes are widely used for many applications, for example, in coatings, paper making, leather tanning, food, textiles, and agriculture.[1,2] However, the anthropogenic addition of these contaminants in the water now poses a significant concern because of their severe health impacts as they are proven carcinogens.[3–5] This imposes a crucial need to develop new, rapid, and advanced remediation approaches capable of removing organic contaminants to provide drinkable water to people. Several physical, chemical, and biological techniques, such as adsorption, absorption, membrane separation, flocculation and coagulation, and electrochemical and catalysis, have been applied recently for the destruction and removal of organic contaminants before their release in wastewater.[4,6–8] Among them, adsorption, an eco-friendly and efficient method, showed a promising route to handle various environmental contaminants.[9,10] Nonetheless, eliminating organic dyes from industrial water is still challenging due to possible by-product formation.[11,12] Therefore, designing new and efficient adsorbent materials to remove organic dyes is highly desirable.

Recently, various adsorbents, including metal oxides, activated carbon, biochar, metal–organic frameworks, *etc.*, have been applied to treat organic dyes in water.[11,13–15] Among them, metal oxides are the most commonly utilized materials to remove contaminants as they are cheap and widely manufactured. Besides, metal oxides exhibit good mechanical properties and resistance to thermal decomposition compared to others.[16] Out of these, alumina oxide adsorbents, such as α-Al_2O_3, γ-Al_2O_3, and γ-AlOOH in various forms, which show eco-friendly nature, cost-effective, are easily synthesized.[11,16–20] Hydrolysis and precipitation are easy, simple, and cost-effective routes for preparing these nanoparticles and their composites. The physicochemical properties of produced materials can be influenced by solvent, concentration, and temperature. Though alumina oxide adsorbents have been commonly used as adsorbent materials, the removal efficiency of these materials toward organic dyes is still not high owing to their low surface area and pore volume.[19,21] To avoid these problems, there have been many studies on the modification of alumina to improve their physicochemical properties, enhancing adsorption. For instance, Ibrahim *et al.* prepared a Cr_2O_3–Al_2O_3 composite and found that the material exhibited improved adsorption ability toward Congo red dye.[22] Recently, Barakat *et al.* developed an Al_2O_3/GO/halloysite nanotube composite with improved

---

[a] *Faculty of Chemical Engineering, Ho Chi Minh City University of Food Industry, 140 Le Trong Tan, Tan Phu, Ho Chi Minh City, Vietnam*

[b] *University of Education, Hue University, 34 Le Loi, Phu Hoi, Hue City, 530000, Vietnam*

[c] *Department of Chemical Engineering, Industrial University of Ho Chi Minh City, 12 Nguyen Van Bao, Go Vap, Ho Chi Minh City, Vietnam. E-mail: votheky@iuh.edu.vn*

removal efficiency toward methylene blue and congo red dyes from wastewater. Singh *et al.* synthesized an Al_2O_3/GO cellulose-based 3D-hydrogel that showed enhanced adsorption ability compared to the bare Al_2O_3.[23] Ding *et al.* prepared an Al_2O_3–TiO_2 nanocomposite with enhanced adsorption performance to uranium from an aqueous solution.[19] Despite many efforts, research on tailoring alumina oxide structures to improve their physicochemical properties and porosity is still limited.

Developing a highly efficient, cost-effective, and eco-friendly method for material preparation is also a critical issue, particularly when considering applying the material in the industry. So far, most materials have been prepared using batch mode synthesis, which usually requires a very long holding time and is challenging to scale.[24–26] Recently, research has shown that spray pyrolysis has a high potential and advantage for preparing metal oxides as it is versatile, rapid, and scalable.[27–31] The spray pyrolysis process includes four main steps: (i) generation of droplets from precursor solution, (ii) shrinkage of droplets, (iii) conversion of precursors to metal oxides, and (iv) solid particle formation.[27,32] In addition, our previous work indicated that γ-Al_2O_3 microspheres prepared by spray pyrolysis exhibited considerably improved surface area and pore volume compared to that derived by the conventional precipitation method.[24,33]

Herein, various contents of TiO_2 were *in situ* incorporated into γ-Al_2O_3 *via* the spry pyrolysis of boehmite sol and titania sol mixture, producing mesoporous Al_2O_3–TiO_2 microspheres. It was realized that introducing TiO_2 into γ-Al_2O_3 created synergetic effects that reduced the alumina's crystallite size and made more mesoporous structures as well as new active sites. The prepared TiO_2/Al_2O_3 microspheres were first used as adsorbents to remove anionic methyl orange and cationic rhodamine B from water in the batch adsorption process. Then, the impact of environmental conditions, including concentration, pH, and coexisting ions, was systematically studied to optimize the removal efficiency. Finally, TiO_2/Al_2O_3 microspheres were further tested for the continuous flow column adsorption of dyes to confirm the applicability of spray pyrolysis-derived TiO_2/Al_2O_3 microspheres.

2. Experimental

2.1. Synthesis of TiO_2/Al_2O_3 microspheres

Multi-grams of mesoporous microspheres, Al_2O_3, TiO_2, and TiO_2/Al_2O_3, were rapidly prepared by spray pyrolysis approach according to our previous work.[25] First, stable boehmite sol and titania sol (0.25 M) were prepared by hydrolysis of aluminium isopropoxide and titania isopropoxide precursors, respectively. For spray pyrolysis, the calculated volumes of these solutions were mixed under constant stirring conditions. To the mixture, citric acid (CA), being a surfactant, was added to enhance the surface area and pore volume of the produced materials. The sol mixture was then transferred into a nebulizer to produce fine sol droplets before entering into a quartz column heated at 650 °C utilizing an air flow (Scheme 1). The resulting product was collected and heated in the air for 2 h to eliminate carbonaceous materials. The obtained microspheres were named TiO_2/Al_2O_3 #*x*, where *x* is the weight percentage of TiO_2.

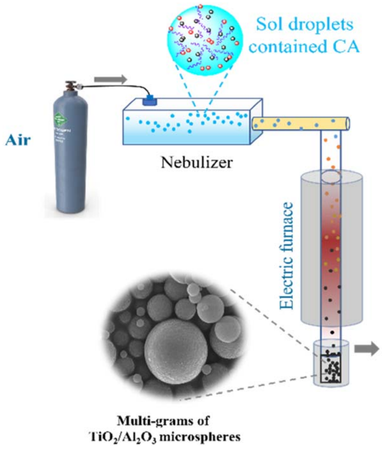

Scheme 1 The schematic diagram for the spray pyrolysis synthesis of TiO_2/Al_2O_3 microspheres.

2.2. Characterization

Electron micrographs of the prepared materials were collected by field-emission scanning electron microscopy (FE-SEM; Leo-Supra 55, Carl Zeiss STM, Germany) and TEM (Talos F200X). The specific area, pore volume, and pore size distribution of the prepared catalysts were determined using N_2 porosimetry (ASAP 2020, Micromeritics Instrument Co., USA) at 77 K. Before measurements, the samples were activated at 450 K for 8 h. The surface areas of the materials were calculated using the Brunauer–Emmett–Teller (BET) equation. The Barrett–Joyner–Halender (BJH) approach with cylindrical pore size was estimated from the Kelvin equation. X-ray diffraction patterns were obtained by powder X-ray diffractometer (PXRD; MAC-18XHF, Rigaku, Japan) using a Cu Kα radiation source ($\lambda = 1.54$ Å). Further, the functional groups of the materials were recorded using FT-IR spectroscopy (Tensor 27, Bruker, Germany). The zeta potential was measured using ZETASIZER Nano-ZS from Malvern Instruments.

Ammonia temperature-programmed desorption (NH_3-TPD) measurements were conducted to explore the acidic properties of the materials. First, the samples were pretreated at 500 °C for 1.5 h under He flow to eliminate the adsorbed moisture from the microspheres, followed by cooling to 115 °C. Afterwards, the materials were ammonia-saturated in a stream of 60 cm^3 NH_3 for 1 h. Finally, physically adsorbed NH_3 was desorbed using a He flow of 60 cm^3 min^{-1} for 4 h, and temperature increased from 100 °C to 900 °C with a heating rate of 10 °C min^{-1}.

2.3. Adsorption experiments

2.3.1. **Batch adsorption.** The adsorption ability of the produced materials was elucidated using anionic methyl orange and cationic rhodamine B as simulated pollutants. For each run, 15 mg of degassed adsorbent was introduced in a 50 mL dye solution at the desired concentration and pH value with constant stirring at ambient temperature. The pH of the solution was adjusted by adding NaOH (0.15 M) or HCl (0.15 M) solutions. At regular intervals, the solution was withdrawn and filtered, and the dye concentration in the filtrates was determined using UV-vis spectroscopy (Optizen POP, Mecasys, Korea). The adsorption capacity of adsorbents was calculated using eqn (1):

$$q = \frac{(C_0 - C_e) \times V}{m} \tag{1}$$

where C_0 and C_e (mg L^{-1}) represent the initial and equilibrium concentrations of the contaminant, respectively; V (L), m (g), and q (mg g^{-1}) are the volume of the solution, the adsorbent's weight, and the adsorption capacity, respectively.

2.3.2. **Continuous flow adsorption.** The continuous flow tests were carried out utilizing a column setup. A buret (48.6 cm × 1.2 cm) was used as the column, filled sequentially with a sponge, quartz sand (18 g), sand-adsorbent mixture (10 g + 1.8 g of adsorbent), quartz sand (18 g), and sponge. The column was packed and sealed with a pressurized rubber cork from the top end. For each run, dye solution prepared with a concentration of 40 mg L^{-1} and pH of 5.5 was passed in the column at a flow rate of 0.5 mL min^{-1} using a peristaltic pump. Herein, the flow direction was kept upward to achieve homogeneous contact. The elute was collected regularly and analyzed for effluents' contents. For the blank experiment, a sand quartz column was used.

3. Results and discussion

3.1. Characterization

Fig. 1(a–f) show the SEM and TEM images of Al_2O_3, TiO_2/Al_2O_3, and TiO_2 samples derived by spray pyrolysis. All samples are uniform spherical particles with diameters ranging from 0.3–2.5 μm. EDS mapping analysis revealed the existence of Al, O, and Ti species, which were well dispersed through the microspheres [Fig. 1(g and h)]. The crystallography analysis of all materials was performed, and the results are presented in Fig. 2(a). As shown, the XRD pattern obtained for the bare alumina and titania implies the formation of γ-Al_2O_3 and TiO_2 anatase, respectively. For the TiO_2-modified Al_2O_3 samples, the XRD patterns of TiO_2/Al_2O_3 #5 and TiO_2/Al_2O_3 #15 samples show only peaks of γ-Al_2O_3 but no sign of TiO_2. This could be because the newly formed TiO_2 particles were finely incorporated within the γ-Al_2O_3 matrix during the spray pyrolysis or could exist in the amorphous phase and beyond the XRD detection. Nonetheless, the XRD pattern of TiO_2/Al_2O_3 #25 exhibits the peaks of TiO_2 anatase at 2θ ~25.4°. This suggests that TiO_2 might grow well and agglomerate onto the surface of γ-Al_2O_3 at such a high content. Furthermore, the peaks of Al_2O_3 were observed to shift slightly and were broader [see the inset Fig. 2(a)], suggesting the incorporated titania could increase lattice strain and reduce the particle size of alumina. Indeed, the particle size of γ-Al_2O_3 was estimated by applying the Scherrer formula, and obtained results are presented in Table 1. As shown, the bare γ-Al_2O_3 had a crystallite size of *ca.* ~3.75 nm; meanwhile, the crystallite size of Al_2O_3 in the composite TiO_2/Al_2O_3 #5 and TiO_2/Al_2O_3 #15 was *ca.* ~3.60 and ~3.44 nm, respectively. However, loading higher TiO_2 content, up to 25 wt%, did not affect the crystallite size of Al_2O_3.

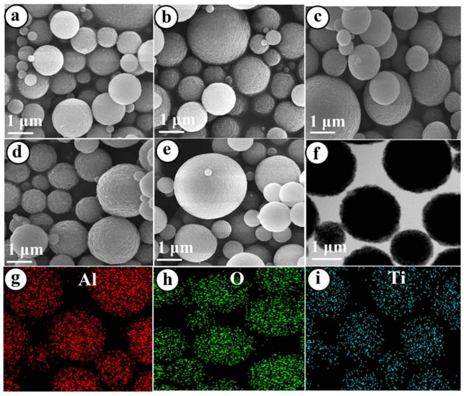

Fig. 1 SEM images of the sample (a) Al_2O_3, (b) TiO_2/Al_2O_3 #5, (c) TiO_2/Al_2O_3 #15, (d) TiO_2/Al_2O_3 #25, (e) TiO_2; (f) TEM image of TiO_2/Al_2O_3 #15 and EDS mapping analysis of (g) Al, (h) O, and (i) Ti of the TiO_2/Al_2O_3 #15 sample.

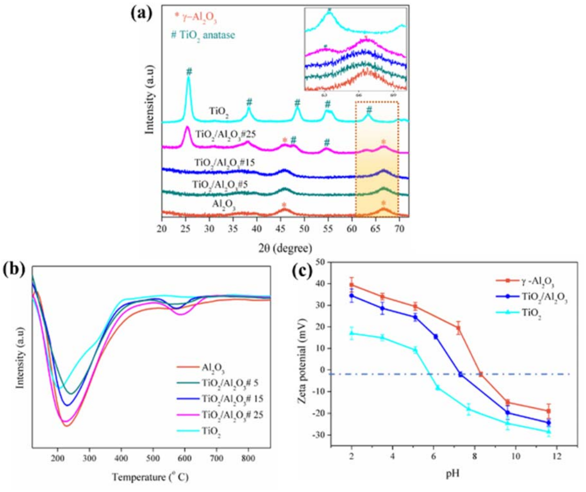

Fig. 2 (a) XRD, (b) H_3N-TPD profile, and (c) zeta potential measurements for the prepared samples.

The temperature-programmed desorption of NH_3 was performed to evaluate the materials' content and types of acid sites. As demonstrated in Fig. 2(b), the TPD profile of the bare γ-Al_2O_3 and TiO_2 exhibits a desorption peak of NH_3 at a low temperature of ~200 °C and 227 °C, respectively, which are ascribed to their weak acid sites. For the TiO_2/Al_2O_3 composite, the TPD curve shows NH_3 desorption peaks at approximately 230 °C and 578 °C, assigned to weak and strong acid sites, respectively. The results indicate that incorporating TiO_2 into γ-Al_2O_3 generated more acid sites owing to the added Ti^{4+} sites or the newly formed bonds (*e.g.*, –Al–O–Ti–) in the composite materials.[24,34] Because of the electrostatic force, these acid sites would enhance the materials' adsorption ability toward anionic dyes. The acid density of the prepared materials was obtained by dividing total acid sites by surface area. Accordingly, the highest acid density of *ca.* ~3.89 μmol m^{-2} was achieved for the synthesized TiO_2/Al_2O_3 #15 sample. Moreover, the zeta potential and point of zero charges (pH_{PZC}) of the spray pyrolysis-derived

Table 1 Crystallite size, surface area, and volume of the samples

Sample	Mean crystallite size of Al_2O_3, nm	BET surface area, $m^2\ g^{-1}$	Total volume, $cm^3\ g^{-1}$	Mean diameter, nm
γ-Al_2O_3	3.75	320	0.31	3.28
TiO_2/Al_2O_3 #5	3.60	298	0.29	3.81
TiO_2/Al_2O_3 #15	3.44	265	0.27	4.14
TiO_2/Al_2O_3 #25	3.77	175	0.25	4.45
TiO_2	—	124	0.18	5.34

microspheres Al_2O_3, Al_2O_3–TiO_2, and TiO_2 were analyzed, and the obtained results are presented in Fig. 2(c). The bare γ-Al_2O_3 and TiO_2 anatase had pH_{PZC} values of ~8.3 and 5.1, respectively. As can be seen that modifying γ-Al_2O_3 with TiO_2 reduced the pH_{PZC} value to ~7.6, indicating the changes in surface chemistry of the Al_2O_3–TiO_2 microspheres due to the incorporated TiO_2 anatase.

N_2 adsorption and pore size distributions of the fabricated adsorbents are presented in Fig. 3(a) and (b), respectively. As revealed in Fig. 3(a), the N_2 adsorption curves of all samples are typical type IV curves with a hysteresis loop, suggesting capillary condensation in mesopores. Table 1 lists the calculated BET surface area and pore volume of the synthesized adsorbents. The bare γ-Al_2O_3 and TiO_2 anatase microspheres had BET surfaces of ~320 $m^2\ g^{-1}$ and ~124 $m^2\ g^{-1}$, respectively. However, incorporating TiO_2 into the alumina matrix decreased the surface area of the adsorbents. Specifically, the surface area of the composite fell from ~298 to 175 $m^2\ g^{-1}$ with increasing TiO_2 content from 5 to 25 wt%, respectively. Noticeably, the modification of γ-Al_2O_3 with TiO_2 by the spray pyrolysis method produced new mesopores and increased the mean pore diameters of the adsorbents, which are beneficial for capturing the organic contaminants.

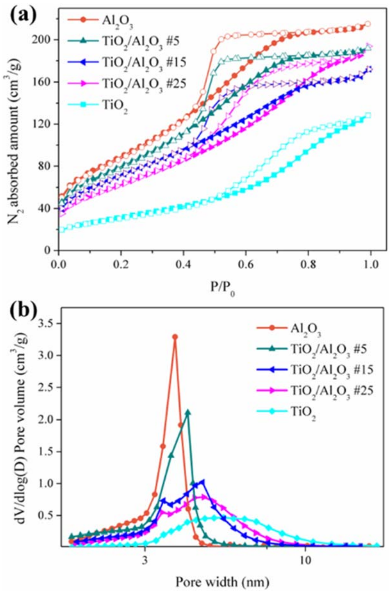

Fig. 3 (a) N_2 adsorption–desorption isotherm, (b) pore size distribution of the synthesized samples.

3.2. Batch adsorption experiments

The synthesized adsorbents were applied to remove the textile dyes, including methyl orange (MO) and rhodamine B (RB). Fig. 4(a–d) show the adsorption data (the discrete points) of contaminants as a function of contact time. As revealed, the adsorption of textile dyes reached equilibrium after approximately 6.5 h for both tested dyes. Furthermore, the results showed that modifying γ-Al_2O_3 with 5–15 wt% TiO_2 increased the composites' adsorption compared to the bare oxide γ-Al_2O_3 and TiO_2 titania despite decreased surface area. This is because adsorption depends on the porosity, adsorbent's particle size, and pore structures. As mentioned above, incorporating TiO_2 generated new mesoporous forms favourable for the diffusion of the contaminants into the pore spaces from the bulk solution. In addition, loading TiO_2 reduced the particle size of Al_2O_3, enhancing the contact area between the adsorbates and the adsorbent's active site and increasing the adsorption capacity. In addition, the TiO_2-incorporated Al_2O_3 composites

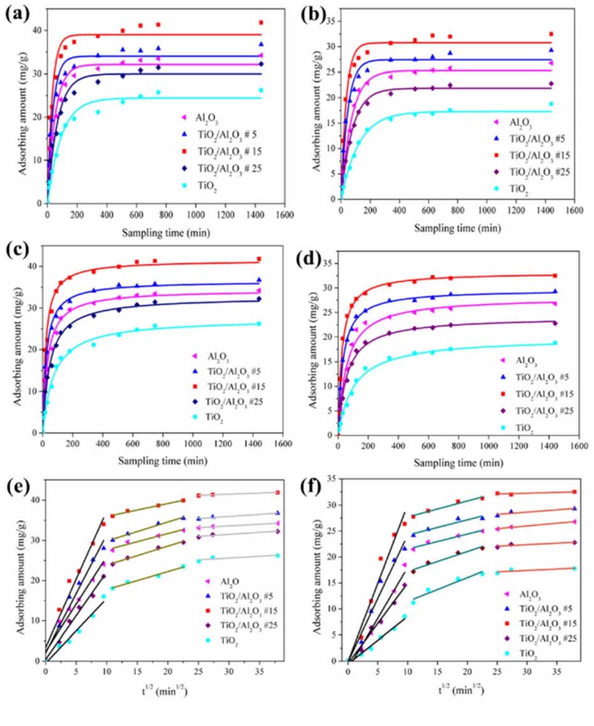

Fig. 4 Pseudo-first order plots for (a) MO and (b) RB, and pseudo-second order (c) MO and (d) RB; intraparticle diffusion model for (e) MO and (f) RB ($C^0_{dye} = 40$ mg L^{-1}, pH = 5.5).

contained new adsorption sites, being proven through ammonia adsorption–desorption, which could also facilitate adsorbate–adsorbent interactions, enhancing the capture of these organic species. That is to say, introducing TiO_2 anatase into the γ-Al_2O_3 host generated a synergistic effect that enhanced the adsorption of dyes onto the TiO_2/Al_2O_3 microspheres. Nonetheless, increasing the TiO_2 dopant content up to 25 wt% diminished the adsorption ability of the adsorbent owing to their significantly reduced porosity. Table 2 compares the removal of MO and RB over various adsorbents, showing that the spray pyrolysis-derived TiO_2/Al_2O_3 microspheres exhibited high adsorption ability towards dyes compared to many counterparts.

The adsorption behaviour of organic contaminants onto the produced adsorbents was uncovered by applying the nonlinear pseudo-first-order and pseudo-second-order models, as presented in Fig. 4(a–d) (the dash lines). The consistency between the experimental data and the models was evaluated *via* the average relative error (ARE), which is defined as follows:[14]

$$\mathrm{ARE} = \sum_{i=1}^{n} \left| \frac{q_{\mathrm{e,exp}} - q_{\mathrm{e,cal}}}{q_{\mathrm{e,exp}}} \right| \tag{2}$$

where $q_{\mathrm{e,exp}}$ and $q_{\mathrm{e,cal}}$ are the experimental and estimated adsorbing amounts (mg g^{-1}), respectively.

The obtained fitted parameters are listed in Table 3. As shown, the higher value of the coefficient R^2 and the lower value of ARE were obtained for the pseudo-second-order, suggesting that this kinetic model described the capture of dyes onto the adsorbents well. Accordingly, the rate constants obtained for the second-order model follow the order $k^{\mathrm{MO}} > k^{\mathrm{RB}}$, indicating that the adsorption rate of MO was faster than RB under the investigated conditions. The rate-limiting adsorption step was determined by applying the intraparticle diffusion (ID) model, which is expressed as follows:[35,36]

$$q_{\mathrm{t}} = k_{\mathrm{ID}} t^{1/2} + C \tag{3}$$

where k_{ID} is the rate constant of the intraparticle diffusion model (mg g^{-1} $min^{-1/2}$), q_{t} is the adsorbing amount (mg g^{-1}), and C is a constant. As shown in Fig. 4(e and f), these obtained ID plots included three separate linear portions, implying three diffusion stages during the adsorption process. The first stage is the external surface diffusion into macro-pores, in which the adsorbents enter into the less accessible spaces, so the diffusion resistance increases, and the diffusion rate decreases. The gradual adsorption step was the second stage, which was governed by intraparticle diffusion. The third stage was the final equilibrium stage, for which the molecules moved slowly from the larger pores to micropores, causing a slow adsorption rate.

Table 2 Removal of MO and RB over various adsorbents

Pollutant	Adsorbent	pH	Adsorption capacity, mg g^{-1}	Ref.
MO	de-Oiled soyga	3.0	13.46	37
	Natural skin almonds	4.0	20.2	38
	Orange peel	>7	20.5	39
	Hyper crosslinked polymeric adsorbent	7	40	40
	γ-Fe_2O_3/SiO_2/chitosan composite	—	37	41
	Spray pyrolysis-derived TiO_2/Al_2O_3 microsphere	5.5	41.15	This work
RB	*Xanthium strumarium* L. seed hull	2	1.7	42
	Microwave-activated rice husk ash	5.5	21.89	43
	Activated carbon from lignocellulosic waste	7	33.3	44
	Hyper crosslinked polymeric adsorbent	7	58	40
	Furfural residue	3.0	37.93	45
	Spray pyrolysis-derived TiO_2/Al_2O_3 microsphere	5.5	32.28	This work

Table 3 Kinetic parameters obtained for MO and RB removal using the prepared adsorbents

			Pseudo-first-order				Pseudo-second-order			
Pollutant	Adsorbent	$q_{\mathrm{e,exp.}}$ (mg g^{-1})	$q_{\mathrm{e,cal}}$ (mg g^{-1})	$k_1 \times 10^2$ (min^{-1})	ARE	R^2	$q_{\mathrm{e,cal}}$ (mg g^{-1})	$k_1 \times 10^2$ (g mg^{-1} min^{-1})	ARE	R^2
MO	Al_2O_3	33.81 ± 3.19	31.98	1.9	7.38	0.932	34.12	0.09	3.33	0.978
	TiO_2/Al_2O_3 #5	35.42 ± 3.67	34.04	2.7	7.27	0.944	36.0	0.12	1.21	0.996
	TiO_2/Al_2O_3 #15	41.15 ± 4.34	39.01	3.2	5.57	0.946	41.03	0.19	3.32	0.995
	TiO_2/Al_2O_3 #25	30.11 ± 2.78	29.18	1.47	4.42	0.961	31.19	0.07	2.12	0.989
	TiO_2	26.42 ± 2.15	24.4	1.09	4.75	0.960	27.08	0.05	2.25	0.985
RB	Al_2O_3	24.52 ± 2.46	23.56	1.38	6.01	0.979	25.07	0.08	3.79	0.989
	TiO_2/Al_2O_3 #5	27.67 ± 2.81	25.89	2.21	4.89	0.977	28.11	0.09	2.28	0.995
	TiO_2/Al_2O_3 #15	32.28 ± 3.89	30.12	2.87	5.56	0.954	33.04	0.11	3.27	0.994
	TiO_2/Al_2O_3 #25	21.87 ± 2.75	19.59	1.29	4.17	0.968	22.34	0.05	3.26	0.986
	TiO_2	18.46 ± 2.04	16.97	0.83	3.98	0.978	19.29	0.03	2.91	0.998

Table 4 The parameters of the intraparticle diffusion model for the adsorption of MO and RB by the synthesized adsorbents

		Stage I		Stage II		Stage III	
Pollutant	Absorbent	k_1 (mg g^{-1} min$^{-1/2}$)	R^2	k^2 (mg g^{-1} min$^{-1/2}$)	R^2	k^3 (mg g^{-1} min$^{-1/2}$)	R^2
MO	Al_2O_3	2.36	0.978	0.31	0.967	0.08	0.991
	TiO_2/Al_2O_3 #5	2.94	0.965	0.39	0.959	0.10	0.973
	TiO_2/Al_2O_3 #15	3.39	0.985	0.42	0.968	0.05	0.968
	TiO_2/Al_2O_3 #25	2.17	0.974	0.47	0.987	0.10	0.971
	TiO_2	1.60	0.994	0.44	0.986	0.09	0.979
RB	Al_2O_3	1.96	0.984	0.24	0.992	0.10	0.993
	TiO_2/Al_2O_3 #5	2.44	0.961	0.29	0.979	0.09	0.985
	TiO_2/Al_2O_3 #15	3.02	0.945	0.33	0.982	0.04	0.974
	TiO_2/Al_2O_3 #25	1.54	0.978	0.39	0.991	0.06	0.986
	TiO_2	0.91	0.994	0.45	0.998	0.05	0.997

As shown in Table 4, the diffusion rate gradually decreased ($k_1 > k_2 > k_3$), implying that the accessible path available for diffusion became narrower and the pores' dimensions diminished.

3.3. Effects of internal factors

Effects of experimental conditions, including the initial concentration of dyes and pH, were investigated using the prepared TiO_2/Al_2O_3 adsorbent. Fig. 5(a and b) show the maximum adsorption capacity of the simulated pollutants as a function of their initial concentrations. As revealed, the adsorbed amounts of textile dyes increased with their starting concentrations. This could be attributed to the enhanced contacting probability between the adsorbents and the adsorbates. In addition, it is noticed that the dye adsorption capacity slowly increased when increasing their initial concentration from 120 to 160 mg L^{-1}, indicating the saturation of the adsorption sites. According to the results, the maximum adsorbed amounts of MO onto the prepared TiO_2/Al_2O_3 #15 were *ca.* ~29.5, 41.15, 47.87, 51.8, and 53.5 mg g^{-1} at concentrations of 20, 40, 80, 120, and 160 mg L^{-1}, respectively; the maximum adsorbed amounts of RB by TiO_2/Al_2O_3 #15 were *ca.* ~19.7, 32.2, 40.7, 46.6, and 47.8 mg g^{-1} at concentrations of 20, 40, 80, 120, and 160 mg L^{-1}, respectively.

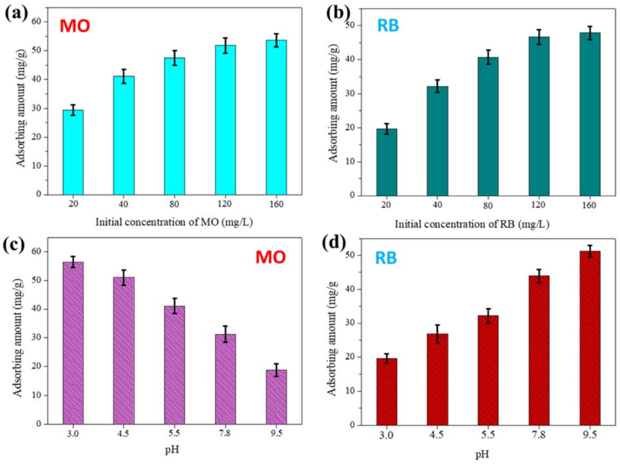

Fig. 5 Effects of (a and b) initial concentration of dyes (pH = 5.5) and (c and d) pH on the adsorption of MO and RB over the TiO_2/Al_2O_3 #15 adsorbent ($C^0_{dye} = 40$ mg L^{-1}).

The adsorbent–adsorbate interaction could be changed by altering the solution pH, leading to a change in removal efficiency. Fig. 5(c and d) show the effects of pH on the adsorption of the investigated textile dyes onto the TiO_2/Al_2O_3 microspheres. As shown, the adsorbing amount of MO decreased; meanwhile, the adsorbing amount of RB increased with an increase in pH, exhibiting pH sensitivity and dependent capture capacity of these molecules. In acidic media, the –OH groups on the surface of the TiO_2/Al_2O_3 spheres were protonated by H^+ ions to form $-OH_2^+$, giving a positively charged surface. Thus, this leads to restricting the approach of cationic RB dye owing to electrostatic repulsion. However, due to electrostatic attraction, the positively charged surface would increasingly attract more anionic MO molecules onto the adsorbent's exterior, enhancing adsorption. Conversely, in basic media, the TiO_2/Al_2O_3 surface was deprotonated by OH^- ions, producing a negatively charged surface favourable for the adsorption of cationic RB species. Besides electrostatic force, the interaction between TiO_2/Al_2O_3 adsorbent materials and dye molecules might include hydrogen bonding.

3.4. Effects of coexisting ions

Industrial effluents usually contain many cations and anions, which would compete with textiles for the active adsorption sites onto the adsorbent. Thus, an efficient material should have a high selectivity toward the adsorbate. Herein, various coexisting anions with the same electric nature as MO, including Cl^-, CO_3^{2-}, HPO_4^{2-}, F^-, NO_3^-, CrO_4^{2-}, and SO_4^{2-} were selected for interference investigation at the designed concentration of 1.5 mmol L^{-1} and 5.0 mmol L^{-1}, respectively. As demonstrated in Fig. 6, the adsorption efficiency of MO dye drops when the concentration of coexisting anions increases from 1.5 mmol L^{-1} to 5 mmol L^{-1}. The presence of monovalent ions, such as F^-, Cl^-, and NO_3^-, did not affect the adsorption performance. Meanwhile, SO_4^{2-} and CrO_4^{2-} were observed to slightly impact the dye removal efficiency, suggesting that these ions would compete with methyl orange molecules for the

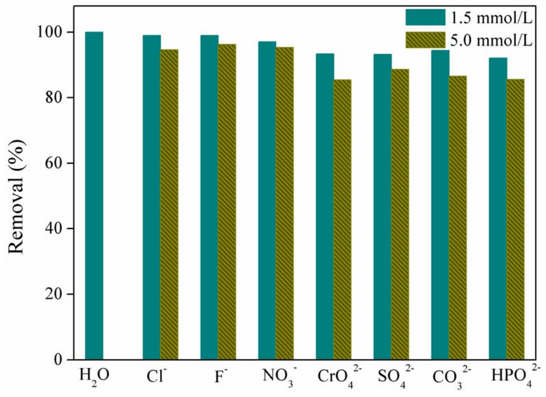

Fig. 6 Effects of coexisting anions on MO adsorption ($C_{MO}{}^0$ = 40 mg L^{-1}, pH = 5.5).

adsorption sites of the adsorbent. This could be because these divalent ions have larger ionic diameters and higher ionic charge density than the above monovalent ions. Overall, the spray pyrolysis-derived TiO_2/Al_2O_3 microspheres exhibited a good adsorption ability towards MO in water containing various coexisting anions.

3.5. Simultaneous removal of dyes

Wastewater released from industry usually contains various textiles. Thus, evaluating the adsorbent's ability to remove multi-dyes in an aqueous solution is necessary. Here, the batch adsorption process was implemented using an equimolar solution of MO and RB (30 mg L^{-1}, pH ∼ 5.5) utilizing the spray pyrolysis-derived TiO_2/Al_2O_3 #15 microspheres. Fig. 7(a) shows the UV-vis spectrum of the solution, and Fig. 7(b) shows the FT-IR spectrum of TiO_2/Al_2O_3 microspheres before and after the adsorption of textile dyes. Results reveal that the MO and RB were simultaneously removed over the TiO_2-incorporated Al_2O_3 microspheres. After 6.5 h, the UV adsorption intensity of MO (λ_{max} = 463 nm) was significantly reduced by approximately 87%, while that of RB (λ_{max} = 554 nm) exhibited a decrease of roughly 32%. The findings suggested that the adsorbent preferentially adsorbed MO much more than the latter contaminant. This can be explained by the fact that MO, an anionic dye, was quickly adsorbed on the positively charged surface of TiO_2/Al_2O_3 owing to the electrostatic attraction force. Moreover, the newly generated acid sites (*e.g.*, Ti^{4+}) of the composite could also contribute to the enhanced capture of anionic dyes.

Conversely, RB, a cationic dye, would not be favourable for adsorption onto the adsorbent because of the electrostatic repulsive force. Besides, the different adsorption behaviour of MO and RB onto the TiO_2-incorporated Al_2O_3 microsphere could be attributed to their differences in chemical structures and molecular sizes. Indeed, pore/size-selective adsorption, monitored by the adsorbate molecule magnitude and adsorbent dimensions, is reportedly an effective adsorption mechanism.[14,46] Herein, methyl orange has a molecular size of ∼1.2 nm, which is smaller than RB (∼1.8 nm).[47] Therefore, MO is more likely to access the pores to occupy the adsorption sites of TiO_2/Al_2O_3 microspheres, leading to the adsorption selectivity of the produced adsorbent. The proposed mechanism for the simultaneous adsorption of MO and RB onto the synthesized TiO_2/Al_2O_3 microspheres is described in Fig. 7(c).

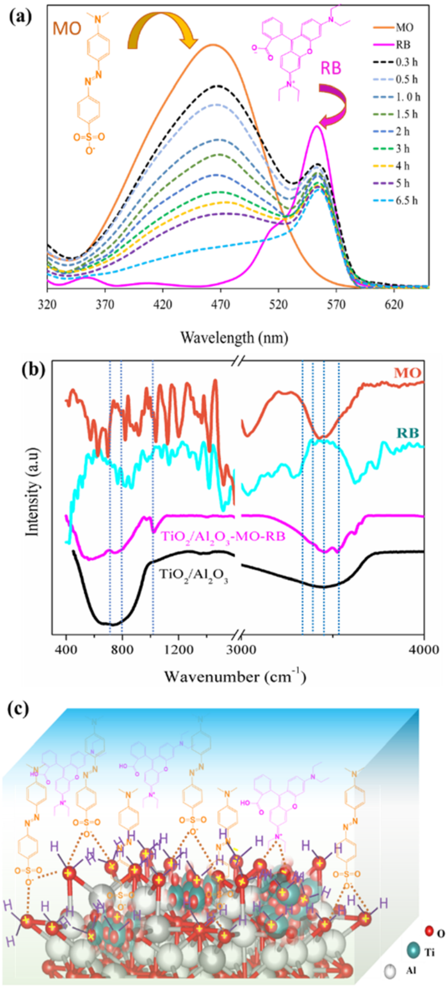

Fig. 7 (a) UV-vis spectrum of the MO-RB solution and (b) FT-IR analyses of the TiO_2/Al_2O_3 adsorbent before and after adsorption; (c) proposed competitive adsorption between MO and RB on the TiO_2/Al_2O_3 microsphere (C^0_{dye} = 30 mg L^{-1}, pH = 5.5).

3.6. Contaminant removal in a continuous flow

The applicability of the produced TiO_2/Al_2O_3 microspheres was further tested using continuous flow column setups, as illustrated in Fig. 8(a and b). As shown, the pollutants quickly passed through the column when using the blank sand bed column. For the column packed with sand and TiO_2/Al_2O_3 mixture, the breakthrough point of the tested MO and RB is approximately ∼150 min and ∼120 min, respectively. The results indicated that the prepared TiO_2/Al_2O_3 effectively removed pollutants in either batch or continuous mode. The obtained experimental data were then fitted with the Thomas and Yan models, which have been widely applied to the column behaviour of adsorbent–adsorbate systems:[17,48]

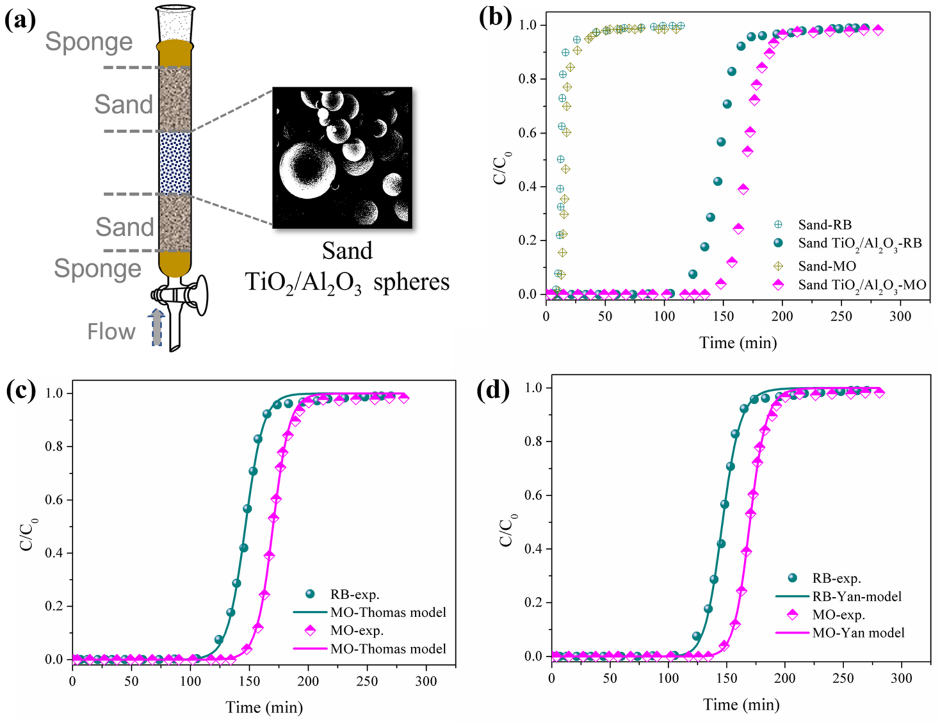

Fig. 8 (a) Schematic diagram for the continuous flow column adsorption using TiO_2/Al_2O_3 microspheres, (b) breakthrough curve results of MO and RB, and (c and d) Thomas and Yan models of the adsorption of dyes.

$$\frac{C_i}{C_0} = 1 - \frac{1}{1 + \left(\frac{C_0 F}{Q_Y} t\right)^{A_Y}} \tag{4}$$

$$\frac{C_i}{C_0} = \frac{1}{1 + \exp\left(\frac{K_{Th} Q_{Th} m}{F} - K_{Th} C_0 t\right)} \tag{5}$$

where t is the sampling time (in min), A_Y and K_{Th} are the constants of the Yan and Thomas models, respectively; Q_Y and Q_{Th} (mg g^{-1}) are the adsorbing capacities estimated by the Yan and Thomas models, respectively. The experimental data were fitted to eqn (4) and (5) *via* nonlinear least square fitting. The mathematical modelling of the textile dye adsorption on the spray pyrolysis-derived TiO_2/Al_2O_3 adsorbents is presented in Fig. 8(c and d) and Table 5. It can be seen that the high R^2 values and low SSE values were achieved for both models, and the estimated Q_Y and Q_{Th} values are very close to the experimental values. These results suggest that the applied models describe well the adsorption behaviour of both contaminants on the mesoporous TiO_2/Al_2O_3 microspheres. The results in Table 5 show that the modelled sorption capacities of ~31 mg g^{-1} and ~19 mg g^{-1} for MO and RB, respectively. This states that it needs 1.0 g of TiO_2/Al_2O_3 microspheres to purify approximately 31 L and 19 L of drinking water contaminated with 1 mg L^{-1} of textile dyes, respectively, in a continuous flow process.

Table 5 Parameters obtained for the column transport models using TiO_2/Al_2O_3 #15 adsorbent

	Thomas model			Yuan model		
Pollutant	Q_{Th}, mg g^{-1}	R^2	SSE	Q_Y, mg g^{-1}	R^2	SSE
MO	30.79	0.998	0.041	30.77	0.998	0.052
RB	19.14	0.997	0.062	19.11	0.996	0.073

4. Conclusions

This study shows that TiO_2-incorporated Al_2O_3 microspheres were rapidly and effectively synthesized by combining sol–gel and spray pyrolysis approaches. The prepared TiO_2/Al_2O_3 microspheres are uniform spherical particles with diameters ranging from 0.5–2.5 μm. With increasing TiO_2 content from 5 to 25 wt%, the surface area reduced from 298 m^2 g^{-1} to 175 m^2 g^{-1}, while the mean pore diameter increased from 3.81 to 4.45 nm, respectively. Furthermore, loading low TiO_2 contents (5–15 wt%) reduced the crystallite size of the Al_2O_3 host. Dye adsorption in batch modes shows that loading 5 to 15 wt% TiO_2 content enhanced the adsorption ability of the adsorbent compared to the bare metal oxides because of the reduced particle size of Al_2O_3, newly formed pore structures, and active sites. Furthermore, introducing TiO_2 into Al_2O_3 created more active sites, enhancing the adsorption performance. The pH media significantly impacted the adsorption performance of TiO_2/Al_2O_3 microspheres; meanwhile, adding the coexisting anions with a concentration range of 1.5–5.0 mmol L^{-1} caused insignificant effects. Notably, TiO_2/Al_2O_3 microspheres showed a higher adsorption selectivity towards anionic MO than cationic RB dye in acidic media. The dye adsorption in continuous flow column processes indicates that the adsorption of MO and RB onto the TiO_2/Al_2O_3 microspheres was described well by the Thomas and Yan models, and the adsorbing capacity of MO and RB was ~31 mg g^{-1} and ~19 mg g^{-1}, respectively. The findings suggest that the TiO_2/Al_2O_3 microspheres can be promising adsorption materials for treating organic pollutants in water.

Conflicts of interest

There are no conflicts to declare.

Acknowledgements

The authors also thank Professor Jinsoo Kim at the Chemical Engineering Department, Kyung Hee University, Korea, for sample analysis. The authors also thank you for the financial support from the Industrial University of Ho Chi Minh City and Ho Chi Minh City University of Food Industry.

References

1 M. Madkour and F. Al Sagheer, *Opt. Mater. Express*, 2017, **7**, 158–169.
2 R. Nivedhitha and S. Velmurugan, *Int. J. Chem. Pharm. Sci.*, 2015, **6**, 18–21.
3 R. Koutavarapu, M. R. Tamtam, M. Rao, S. G. Peera and J. Shim, *Chemosphere*, 2021, **272**, 129849.
4 J. Wang, Q. Zhang, X. Shao, J. Ma and G. Tian, *Chemosphere*, 2018, **207**, 377–384.
5 T. K. Vo and J. Kim, *Korean J. Chem. Eng.*, 2020, **37**, 571–575.
6 T. K. Vo, J.-H. Kim, H. T. Kwon and J. Kim, *J. Ind. Eng. Chem.*, 2019, **80**, 345–351.
7 H. A. L. Pham, T. K. Vo, D. T. Nguyen, H. K. Huynh, Q. T. S. Pham and V. C. Nguyen, *Green Chem. Lett. Rev.*, 2022, **15**, 572–581.
8 T. K. Vo, M. T. Nguyen, V. C. Nguyen and J. Kim, *Korean J. Chem. Eng.*, 2022, **39**, 2532–2541.
9 X. You, R. Zhou, Y. Zhu, D. Bu and D. Cheng, *J. Hazard. Mater.*, 2022, **430**, 128445.
10 M. E. El-Naggar, E. K. Radwan, H. R. M. Rashdan, S. T. El-Wakeel, A. A. Koryam and A. Sabt, *RSC Adv.*, 2022, **12**, 18923–18935.
11 S. Ali, Y. Abbas, Z. Zuhra and I. S. Butler, *Nanoscale Adv.*, 2019, **1**, 213–218.
12 C. N. Britos, J. E. Gianolini, H. Portillo and J. A. Trelles, *Biocatal. Agric. Biotechnol.*, 2018, **14**, 221–227.
13 B. Qiu, Q. Shao, J. Shi, C. Yang and H. Chu, *Sep. Purif. Technol.*, 2022, **300**, 121925.
14 T. K. Vo, T. P. Trinh, V. C. Nguyen and J. Kim, *J. Ind. Eng. Chem.*, 2021, **95**, 224–234.
15 K. Maru, S. Kalla and R. Jangir, *New J. Chem.*, 2022, **46**, 3054–3072.
16 J. S. Yamani, A. W. Lounsbury and J. B. Zimmerman, *Water Res.*, 2014, **50**, 373–381.
17 N. Khandelwal, E. Tiwari, N. Singh and G. K. Darbha, *ACS ES&T Water*, 2021, **1**, 641–652.
18 F. Ezati, E. Sepehr and F. Ahmadi, *Sci. Rep.*, 2021, **11**, 18831.
19 L. Ding, T. Xiong, Z. Zhao, J. Liao and Y. Zhang, *J. Mol. Liq.*, 2022, **362**, 119731.
20 V. The Ky, *Int. J. Environ. Anal. Chem.*, 2022, 1–21, DOI: 10.1080/03067319.2021.2023512.
21 W. Zhang, S. Zhang, J. Wang, M. Wang, Q. He, J. Song, H. Wang and J. Zhou, *Chemosphere*, 2018, **203**, 188–198.
22 M. M. Ibrahim, *J. Environ. Chem. Eng.*, 2019, **7**, 102848.
23 N. Singh, S. Kumari, N. Goyal and S. Khan, *Environ. Nanotechnol., Monit. Manage.*, 2021, **15**, 100444.
24 T. K. Vo, W.-S. Kim, S.-S. Kim, K. S. Yoo and J. Kim, *Energy Convers. Manage.*, 2018, **158**, 92–102.
25 T. K. Vo, V. N. Le, D. T. Quang and J. Kim, *Microporous Mesoporous Mater.*, 2021, **321**, 111132.
26 T. K. Vo, J. Kim, T. H. Vu, V. C. Nguyen and D. T. Quang, *Sep. Purif. Technol.*, 2022, **283**, 120237.
27 S. C. Tsai, Y. L. Song, C. S. Tsai, C. C. Yang, W. Y. Chiu and H. M. Lin, *J. Mater. Sci.*, 2004, **39**, 3647–3657.
28 L. D. Hafshejani, S. Tangsir, H. Koponen, J. Riikonen, T. Karhunen, U. Tapper, V.-P. Lehto, H. Moazed, A. A. Naseri, A. Hooshmand, J. Jokiniemi, A. Bhatnagar and A. Lähde, *Powder Technol.*, 2016, **298**, 42–49.
29 A. I. Y. Tok, F. Y. C. Boey and X. L. Zhao, *J. Mater. Process. Technol.*, 2006, **178**, 270–273.
30 T. K. Vo, *Environ. Sci. Pollut. Res.*, 2022, **29**, 42991–43003.
31 J. Choi, K. S. Yoo and J. Kim, *Korean J. Chem. Eng.*, 2018, **35**, 2480–2486.
32 J. S. Cho, K. Y. Jung and Y. C. Kang, *Phys. Chem. Chem. Phys.*, 2015, **17**, 1325–1331.
33 T. K. Vo, D. T. Quang and J. Kim, *Catal. Commun.*, 2022, **169**, 106478.
34 T. Rodseanglung, T. Ratana, M. Phongaksorn and S. Tungkamania, *Energy Procedia*, 2015, **79**, 378–384.
35 C. Cheng, J. Deng, B. Lei, A. He, X. Zhang, L. Ma, S. Li and C. Zhao, *J. Hazard. Mater.*, 2013, **263**, 467–478.
36 J. Wang and X. Guo, *Chemosphere*, 2022, **309**, 136732.
37 A. Mittal, A. Malviya, D. Kaur, J. Mittal and L. Kurup, *J. Hazard. Mater.*, 2007, **148**, 229–240.
38 F. Atmani, A. Bensmaili and A. Amrane, *Desalin. Water Treat.*, 2010, **22**, 174–181.
39 G. Annadurai, R.-S. Juang and D.-J. Lee, *J. Hazard. Mater.*, 2002, **92**, 263–274.
40 J.-H. Huang, K.-L. Huang, S.-Q. Liu, A. T. Wang and C. Yan, *Colloids Surf., A*, 2008, **330**, 55–61.
41 H. Y. Zhu, R. Jiang, Y. Q. Fu, J. H. Jiang, L. Xiao and G. M. Zeng, *Appl. Surf. Sci.*, 2011, **258**, 1337–1344.
42 S. Khamparia and D. K. Jaspal, *J. Environ. Manage.*, 2017, **197**, 498–506.
43 N. V. Suc and D. Kim Chi, *J. Dispersion Sci. Technol.*, 2017, **38**, 216–222.
44 V. da Silva Lacerda, J. B. López-Sotelo, A. Correa-Guimarães, S. Hernández-Navarro, M. Sánchez-Báscones, L. M. Navas-Gracia, P. Martín-Ramos and J. Martín-Gil, *J. Environ. Manage.*, 2015, **155**, 67–76.

45 X. Chen, H. Li, W. Liu, X. Zhang, Z. Wu, S. Bi, W. Zhang and H. Zhan, *Colloids Surf., A*, 2019, **583**, 123976.

46 W. Xiong, G. Zeng, Z. Yang, Y. Zhou, C. Zhang, M. Cheng, Y. Liu, L. Hu, J. Wan, C. Zhou, R. Xu and X. Li, *Sci. Total Environ.*, 2018, **627**, 235–244.

47 Q.-y. Wu, H.-q. Liang, M. Li, B.-t. Liu and Z.-k. Xu, *Chin. J. Polym. Sci.*, 2016, **34**, 23–33.

48 T. K. Vo, V. N. Le, D. T. Quang, M. Song, D. Kim and J. Kim, *Microporous Mesoporous Mater.*, 2020, **306**, 110405.